CRYSTAL GROWTH & DESIGN

Article

pubs.acs.org/crystal

Fabricating Necklace-, Tower-, and Rod-Shaped In_2O_3 Nanostructures by Controlling Saturation Kinetics of Catalyst Droplets in a Vapor−Liquid−Solid Process

J. Alberto Ramos Ramón,[†] Ana Cremades,[‡] David Maestre,[‡] Rutilo Silva González,[†] and Umapada Pal*[,†]

[†]Instituto de Física, Benemérita Universidad Autónoma de Puebla, Apdo. Postal J-48, Puebla, Puebla 72570, Mexico

[‡]Departamento de Física de Materiales, Facultad de Ciencias Físicas, Universidad Complutense de Madrid, 28040 Madrid, Spain

Supporting Information

ABSTRACT: We demonstrate the fabrication of necklace-, tower-, and rod-shaped one-dimensional In_2O_3 nanostructures in a large scale and well-controlled manner in a vapor−liquid−solid growth process by controlling only the temperature of precursor evaporation. Scanning electron microscopy, transmission electron microscopy, micro-Raman spectroscopy, and cathodoluminescence techniques have been utilized to evaluate the morphology, fine structure, crystal quality, and defect content in the nanostructures. It has been seen that the morphology of the nanostructures is controlled by the saturation kinetics of catalyst droplets controlled by the rate of dissolution of gaseous precursor, rate of saturation of the liquid catalyst droplet, and the rate of precipitation from it, all of which can be controlled by adjusting the temperature of precursor evaporation. The mechanisms of formation of the nanostructures are discussed considering the surface energy of their crystalline faces. Single-crystalline nature and low defect content of the formed nanostructure make them attractive candidates for optoelectronic applications.

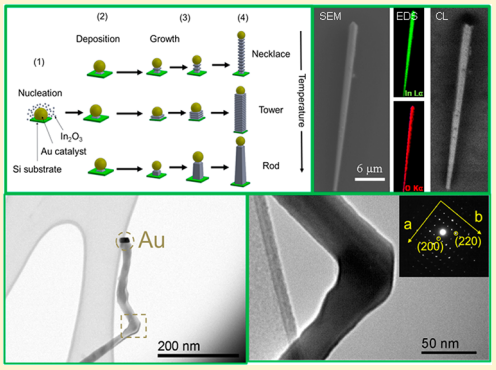

INTRODUCTION

Indium oxide (In_2O_3) is a popular semiconductor with high optical transparency, good electrical conductivity, and high band gap energy (3.5−3.7 eV),[1−4] which has been frequently used for optoelectronic device fabrication.[5] In nanostructure form, In_2O_3 has proven utility in catalysis,[6] fabrication of light emitting diode,[7,8] gas sensing,[9,10] fabrication of field-emission devices,[11] etc. Such attractive potential applications of In_2O_3 nanostructures encouraged researchers to fabricate and characterize their one-dimensional (1D) structures extensively during the last 10 years.[12−17] Different synthesis techniques, such as chemical vapor deposition (CVD),[18] carbothermal reduction,[19] sol−gel,[20] vapor−solid (VS),[21] and vapor−liquid−solid (VLS)[22] have been employed to fabricate 1D In_2O_3 nanostructures. Among the common techniques, VLS has been very popular due to its simplicity, scalability, and solvent-free synthesis process. Although VS and VLS methods have been widely used for fabricating In_2O_3 nanostructures, the dimension and morphology of the obtained nanostructures have been reported to be different for different research groups. For example, Calestani et al.[23] synthesized octahedral-shaped In_2O_3 nanostructures with sharp, truncated tips of 50−120 nm size and nanowires of 30−200 nm thickness and a few hundred micrometers long through a self-catalyzed process. They concluded that although In_2O_3 nanowires can be grown through a self-catalyzed process by controlling the temperature and vapor pressure of the precursor, it is difficult to control their dimensions. Using metallic indium as a precursor and Au as a catalyst, Johnson et al.[22] synthesized In_2O_3 nanowires of 2−10 μm length and 50−100 nm width through the VLS process. The growth rate of the nanostructures was found to be inversely proportional to the vapor pressure of the metallic precursor. Dai et al.[24] synthesized In_2O_3 nanowires of high aspect ratio (20−50 nm diameter and tens of micrometer length), using water-bubbled Ar as an oxidizing agent and metallic indium as a precursor. Formed nanowires were smooth and uniform in diameter without the formation of the tapered end. Furthermore, Magdas et al.[25] could fabricate In_2O_3 micro-/nanostructures of different morphologies by thermal sintering of InN pellets following a VS process. Through one-step sintering of InN pellets at 600 °C, they could fabricate necklace-like structures consisting of stacked pyramidal units connected through nanowires. By sintering the pellets at 700 °C, they obtained a dense mixture of necklace and arrow-type (rods with pyramidal structures at the tips) nano- and microstructures. On the other hand, using a two-step sintering process (sintering at 350 °C for 5 h, followed by another sintering at 600−650 °C for 5 h), they could obtain only 1D structures of uniform morphology. All these reported results indicate that each of the growth parameters such as growth

Received: March 20, 2017
Revised: May 28, 2017
Published: July 17, 2017

DOI: 10.1021/acs.cgd.7b00395
Cryst. Growth Des. 2017, 17, 4596−4602

temperature, chamber pressure, precursor composition, and carrier gas composition have a strong effect on the morphology, dimension, defect, and structural characteristics of the grown In_2O_3 nanostructures. While bulk In_2O_3 does not manifest considerable luminescent emission, In_2O_3 micro-/nanostructures present emissions in the range of 1.9−3.7 eV, depending on their fabrication methods.[26] Emission bands located around 1.90, 2.53, 2.77, and 3.70 eV have been detected for vapor-grown In_2O_3 microstructures,[25] which have been attributed to different oxygen-related defects produced during their growth. Although a considerable effort has been made by researchers to understand the effect of common growth parameters on the morphology, growth rate, and defect structures of In_2O_3 nanostructures,[17,25,26] the understanding is far from complete, mainly due to the large variation of the adapted growth conditions and systems.

With the aim of fabricating In_2O_3 nanostructures of different morphologies by controlling only one growth parameter, we fabricated 1D In_2O_3 nanostructures through the VLS growth process, varying precursor evaporation temperature between 825 and 900 °C for a fixed gas mixture. The effect of the temperature on the morphology, composition, crystal phase, and defect structure of the nanostructures have been studied using scanning and transmission electron microscopies (SEM and TEM), energy dispersive spectroscopy (EDS), X-ray diffraction (XRD), micro-Raman and cathodoluminescence (CL) spectroscopy techniques. The variations of morphology and dimension of the obtained nanostructures have been explained considering their possible growth mechanisms at different temperatures.

EXPERIMENTAL SECTION

In_2O_3 nanostructures were fabricated in a horizontal furnace (Carbolite STF 15/180) through a VLS growth process. A quartz crucible with metallic indium (Sigma-Aldrich, 99.98%) and graphite powder mixture (5:3 w/w) was placed at the center (maximum temperature zone) of the furnace. A Si substrate (1.5 × 1.5 cm^2) covered with ∼20 nm thick sputtered deposited Au film was set facedown over the crucible center, covering it partially. After the quartz tube ends were closed with gas-flow flanges, the temperature of the furnace was raised to the desired value at 37 °C/min heating rate under a constant Ar (99.996% purity) + O_2 (99.999% purity) mixture flow (10:1 v/v, 66 sccm). Prior to heating, the growth chamber (quartz tube) was purged with Ar for 1 h to eliminate residual air. A series of samples was grown by varying the furnace temperature between 825 and 900 °C. After the growth temperature reached its desired value, the growth was continued for 15 min, after which the furnace was cooled down to room temperature naturally. The morphology of the as-grown In_2O_3 nanostructures was analyzed in a JEOL JSM-7800F field-emission scanning electron microscope (FE-SEM) and a FEI Inspect-S SEM. For the analysis of the chemical composition, a Bruker AXS XFlash 4010 X-ray microanalysis system attached to a Leica 440 scanning electron microscope was used. Room temperature X-ray diffraction (XRD) measurements were carried out in a Panalytical XPERT-MPD diffractometer (Cu Kα radiation, λ = 1.54056 Å) to determine the crystal phase of grown nanostructures. Defect content and crystal quality of the grown nanostructures were studied at room temperature through micro-Raman spectroscopy, utilizing a Horiba Lab RAM HR system equipped with a 633 nm He−Ne laser and a thermoelectrically cooled charge-coupled device (CCD) detector and a transmission electron microscope (JEOL JEM 2100) operating at 200 kV. Cathodoluminescence (CL) spectra and images of the In_2O_3 nanostructures were recorded at room temperature utilizing either a Hitachi S-2500 or a Leica 440 SEM equipped with a Hamamatsu PMA-11 charged couple detector (CCD).

RESULTS AND DISCUSSION

After only 15 min of growth, the substrates were fully covered by a significant amount of 1D nanostructures (Figure S1, Supporting Information) which shows the efficiency of the synthesis method. Figure 1 shows the XRD patterns of the as-grown samples. Along with two intense diffraction peaks around 33.02 and 38.30° appearing from the Si substrate, there appeared five sharp peaks around 21.58, 30.70, 35.62, 41.98, 45.86, and 51.18 deg, which belong to In_2O_3 in the cubic phase (JCPDS #760152), with a cell parameter of 10.08 Å. No impurity such as metallic In or other elements/compounds were found in the XRD patterns of the nanostructures. With the increase of growth temperature, while the intensity of the diffraction peaks associated with In_2O_3 increases, indicating their better crystallinity, intensity of the peaks associated with the Si substrate decreases (Figure S2, Supporting Information) due to higher coverage of the substrate by the nanostructures grown at higher temperatures. Figure 2 presents typical SEM images of the In_2O_3 nanostructures obtained at different growth temperatures. As can be seen, the samples predominantly contain elongated nanostructures with different morphologies depending on the growth temperature. For the synthesis at lower temperatures, 1D nanostructures, mainly of necklace-like morphology, are obtained. Figure 2a,b presents some typical SEM images of the nanostructures corresponding to the sample grown at 825 °C. The elongated nanostructures start to grow from microcrystals formed on the substrate, as observed in Figure 2a. These elongated nanostructures are formed by linear arrangement of octahedrons stacked together at their tips. In some cases, these octahedrons do not fully cover the nanowires on which they grow, as appreciable in Figure 2b. The necklace-like nanostructures present lateral sizes of tens of nanometers and lengths of several microns. The presence of spherical catalyst particles, characteristic of the VLS growth process, can be observed at the tip of the nanostructures. The sample grown at 850 °C produced predominant tower-like nanostructures

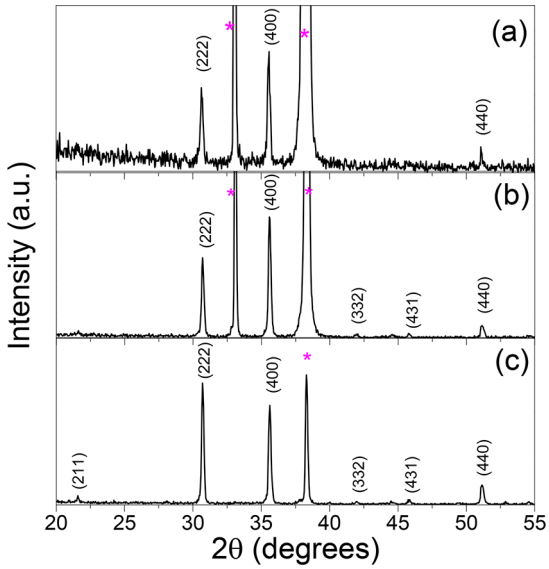

Figure 1. XRD patterns of the samples grown at (a) 825 °C, (b) 850 °C, and (c) 900 °C. Peaks marked with asterisks correspond to the Si substrate utilized as substrate. The decrease of the substrate peak at a higher growth temperature is due to higher coverage of the substrate by In_2O_3 nanostructures.

DOI: 10.1021/acs.cgd.7b00395
Cryst. Growth Des. 2017, 17, 4596−4602

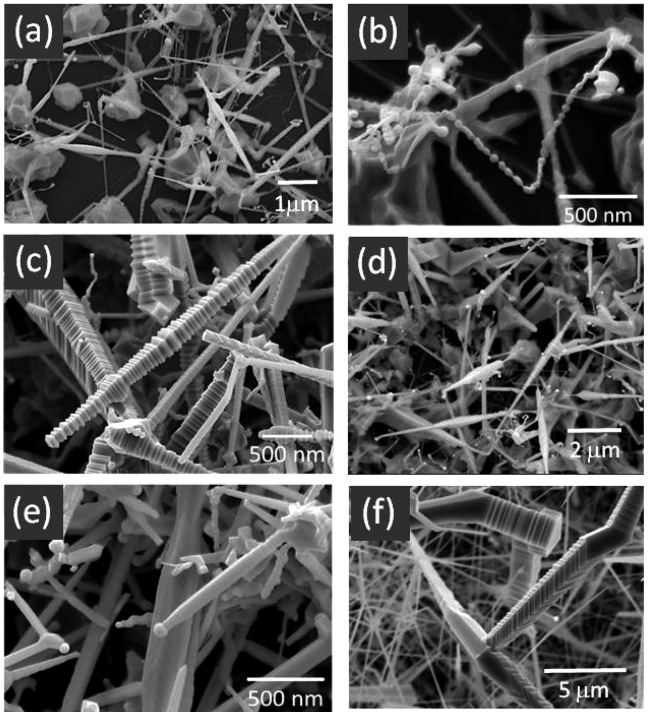

Figure 2. Typical SEM images of VLS-grown In_2O_3 nanostructures fabricated at different temperatures: (a, b) necklace-like nanostructures grown at 825 °C; (c, d) tower-like nanostructures grown at 850 °C; and (e) smooth and (f) stepped surface rod-like nanostructures grown at 900 °C.

(Figure 2c). The multilayered tower structures are formed by stacking of truncated octahedrons of square cross-section. Contrary to the case of necklace-like structures obtained at 825 °C, the tower-like nanostructures are formed by stacked layers of inhomogeneous sizes. While the number of nanostructures grown at this temperature is higher than at 825 °C (Figure 2d), the diameter of the tower-like structures decreases near their tips. For the samples grown at 900 °C, rod-like nanostructures of nearly square cross-section are predominant (Figure 2e). The lateral size of these rods varies between 50 and 200 nm, although occasionally rods of several microns can be observed (Figure 2f). In most of these nanostructures, round-shaped catalyst particles can be observed at their tips. Most of the formed rods contain several segments due to the change in growth direction during formation. The lateral surfaces of these rods appear stepped or flat at the observation scale depending on the considered segment (Figure 2f). Secondary growth is also observed in this case, which leads to interconnection of the rods. It can be noticed that the number of formed nanostructures increases with the increase of growth temperature, due to enhanced evaporation of the indium precursor and higher oxidation rate of indium vapor at higher deposition temperatures.

As can be noticed from Figure 2a,d, some bigger granular crystallites of micrometer sizes are also formed over Si substrate, especially for the samples grown at lower temperatures (825 and 850 °C). Formation of these microcrystals is associated with the involved growth processes. During heating of the precursor (In + C) under Ar + O_2 gas flow, the formation of In_2O_3 nuclei takes place through a VS mechanism, as described by Calestani et al.[23] In fact, as the melting point of indium (In) is lower than the melting point of Au (used as catalyst), and its vapor pressure is higher than gold, it starts evaporating at lower temperature, and the oxidized indium vapor solidifies over the Si substrate at the initial stage of the growth process, while the Au catalyst still remains in the solid state, or the formed Au droplets (molten) have very low solubility. Once the Au droplets are at higher temperature, their solubility increases (for dissolving In_2O_3 vapor), and the VLS growth process starts, which remains as the predominant process for the growth of the nanostructures.

In Figure 3, EDS mappings of representative necklace-, tower-, and rod-like nanostructures are presented, where an

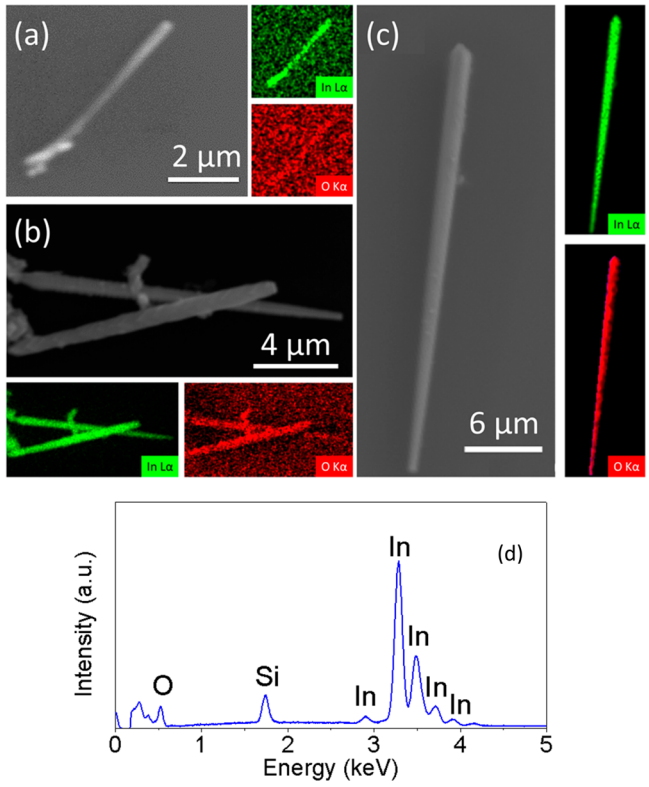

Figure 3. EDS mapping of (a) necklace-like, (b) tower-like, and (c) rod-like In_2O_3 nanostructures, showing a homogeneous distribution of elements in them. (d) Representative EDS spectrum of the In_2O_3 nanostructures (the peak at 1.74 keV corresponds to Si wafer utilized as substrate).

uniform distribution of In and O along the structures can be seen. EDS spectra of the samples revealed their composition with about 69.66 atom % of O and 30.34 atom % of In, which is close to the stoichiometric value for In_2O_3. No other element other than In and O could be detected in the EDS spectra of the nanostructures (Figure 3d), indicating their high purity.

In order to analyze the crystallinity of the grown nanostructures, TEM measurements were carried out on representative structures of the samples grown at different temperatures. The nanostructures were scratched out of the Si substrate, and the material obtained was dispersed in 5 mL of 2-propanol. The dissolutions were sonicated for 15 min in three steps of 5 min each. Two drops of each suspension were deposited on carbon coated Cu grids. The TEM images and selected-area electron diffraction (SAED) patterns of the selected nanostructures are displayed in Figure 3, revealing their single-crystal nature. The SAED patterns of all the nanostructures reveled their body centered cubic phase

DOI: 10.1021/acs.cgd.7b00395
Cryst. Growth Des. 2017, 17, 4596−4602

(JCPDS #760152) with a cell parameter of 10.09 Å, which is in good agreement with their XRD results. The growth direction of most of the nanostructures extends along the [100] direction. Formation of a well crystalline nanowire presenting elbows due to a change in the growth direction can be seen in Figure 4a. Existence of Au catalyst particles can also be

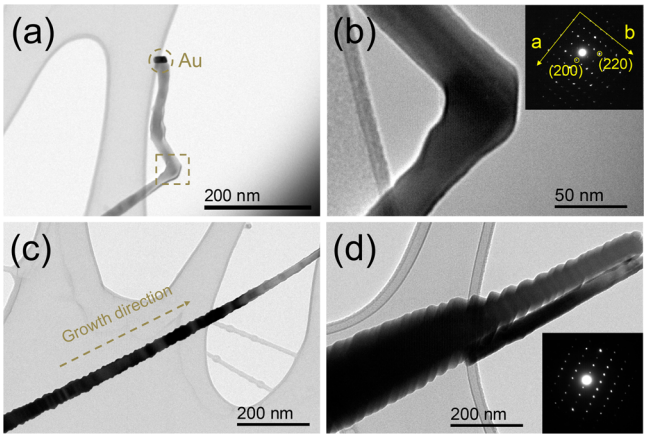

Figure 4. (a) Low-resolution TEM images of an In_2O_3 nanostructure with Au particle at the tip. The elbow region marked in (a) is enlarged in (b). The inset in (b) corresponds to the SAED pattern acquired at the lower branch of the structure. Nanostructures with tower-like morphology are shown in (c) and (d). Inset in (d) corresponds to the SAED pattern acquired at the tip of the nanostructure presented in (d).

observed at its growth front. The magnified image of the elbow (marked by square in Figure 4a) and its SAED pattern are shown in Figure 4b and its inset, respectively. As can be seen from the SAED pattern of the elbow region (lower branch), even at this region the nanostructure preserves its single crystalline nature. While the lower segment of the nanostructure grows along the [100] direction, the upper segment grows along [110]. TEM analyses of the nanostructures do not indicate the presence of any dislocation, or formation of nanopipes in the core of the elongated structures, as usually observed for nanorods grown by the VS process.[27] Therefore, the conventional dislocation-assisted growth mechanism, commonly considered for bent In_2O_3 nanostructures grown by the VS process, cannot be applied for the nanostructures fabricated in this study. Stepped lateral surfaces are also observed in the nanostructures (Figure 4c,d). A more detailed study indicates that these stepped surfaces correspond to the stacking of truncated octahedral units, as can be observed in the nanostructure presented in Figure 4d. The cross-section of these tower-like nanostructures gradually decreases toward their tips (Figure 4d). However, the single-crystal nature of the nanostructures is maintained even at their tips, as can be observed from the SAED pattern acquired near the tip, presented as the inset of Figure 4d.

For qualitative evaluation of crystal quality and defect content in the grown nanostructures, their micro-Raman spectra were recorded at room temperature in the 100−700 cm^{-1} range (Figure 5). The measurements were performed using a 100× objective lens with a laser beam spot size of ∼4.0 μm focused over a single nanostructure. All the structures revealed five well-resolved Raman modes located around 130 (ν_1), 305 (ν_2), 365 (ν_3), 495 (ν_4), and 629 cm^{-1} (ν_5) and two weaker bands around 109 and 154 cm^{-1}, all of which

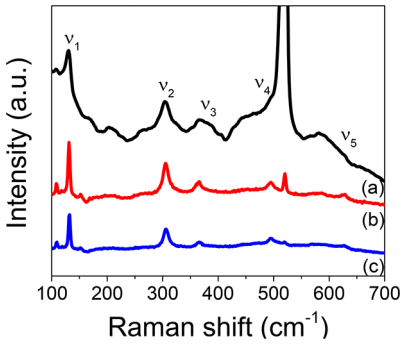

Figure 5. Raman spectra of (a) necklace-, (b) tower-, and (c) rod-like In_2O_3 nanostructures grown at 825, 850, and 900 °C, respectively. The peak at 520 cm^{-1} corresponds to the Si utilized as substrate.

correspond to In_2O_3 in the bcc phase.[17] The peak appearing around 520 cm^{-1} corresponds to the Si wafer used as the substrate. A higher relative intensity of this peak for the sample grown at 825 °C is due to the lower concentration (number per unit area) of the formed nanostructures in comparison to the samples grown at higher temperatures. The vibrational modes appearing around 109, 154, 305, 365, and 629 cm^{-1} correspond to T_g symmetry, while the bands appearing at 130 and 495 cm^{-1} have A_g symmetry. For the necklace-like nanostructures (Figure 5a), two additional modes appeared around 435 and 581 cm^{-1}, which have been observed previously for In_2O_3 octahedrons.[28] As demonstrated by Yin et al.[29] through Raman study, the vibrational properties of In_2O_3 micro- and nanostructures depend on their morphology, especially their sizes and shapes. A change in morphology therefore can induce a change in the relative intensity of their vibrational modes. As our necklace-like nanostructures (grown at 825 °C) are formed by octahedrons connected through their tips, we can expect some of the vibrational modes associated with octahedral crystals in their Raman spectra. Besides, the vibrational modes are broader for the necklace-like nanostructures as they were grown at lower temperature and therefore exhibit lower dimensions than the nanostructures of rod-like morphology. The lower growth temperature of the necklace-like nanostructures causes them to be shorter and wider than the tower- or the rod-like nanostructures. In Table 1, the position and full width at half-maximum (fwhm) of the main vibrational modes of the nanostructures grown at different temperatures are presented. It can be noticed that for higher growth temperatures, the values of fwhm of the vibrational modes reduces. Better crystallization of the nanostructures is expected when the deposition temperature is increased due to the higher evaporation/oxidation rates and solubility of In_2O_3 in catalyst droplets. However, smaller nanostructure dimensions (length and width) cause higher light scattering of the incident laser beam, which also leads to peak broadening in Raman spectrum of necklace-like nanostructures.

Room temperature CL images and spectra of the nanostructures grown at different temperatures are presented in Figure 6 and Figure 7, respectively. As can be seen in Figure 6, the CL images of the nanostructures are monotonous, with almost uniform distribution of CL intensity along their lengths, indicating the apparent absence of nonradiative extended defects such as dislocations or stacking faults, or if they exist, they could not be detected within the resolution limit of the used system. On the other hand, the CL spectra of the nanostructures (Figure 7) revealed only one intense and broad

DOI: 10.1021/acs.cgd.7b00395
Cryst. Growth Des. 2017, 17, 4596−4602

Table 1. Position and FWHM, in Brackets, of the Main Vibrational Modes of In_2O_3 Nanostructures Grown at Different Temperatures

	peak positions (fwhm) (cm^{-1})					
morphology/growth temperature	A_g	T_{2g}	T_{2g}	A_g	A_g	T_{2g}
necklace-like, 825 °C	131 (10.5)	306 (41.7)	369 (69.0)	469 (100.2)	511 (12.0)	642 (175.0)
tower-like, 850 °C	132 (3.8)	306 (11.5)	365 (15.9)	457 (71.1)	495 (16.9)	628 (14.2)
rod-like, 900 °C	131 (3.5)	306 (11.0)	366 (12.4)	466 (56.4)	499 (15.6)	626 (27.4)

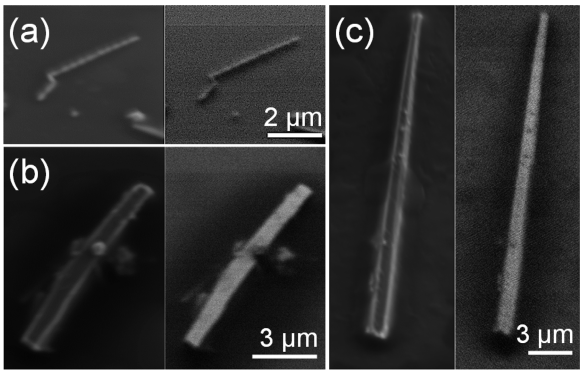

Figure 6. Typical SEM (left) and CL (right) images acquired at room temperature on nanostructures grown at (a) 825 °C, (b) 850 °C, and (c) 900 °C.

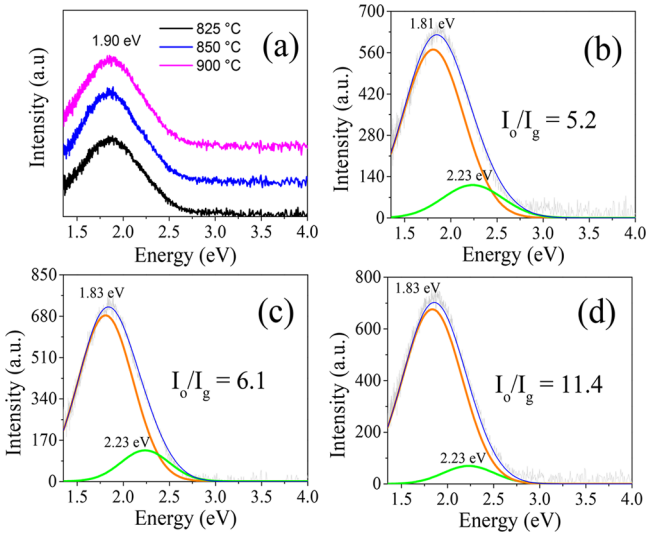

Figure 7. (a) Room temperature CL spectra of the samples grown at different temperatures. Deconvoluted CL spectra of (b) necklace-, (c) tower-, and (d) rod-like In_2O_3 nanostructures grown at 825, 850, and 900 °C, respectively.

emission band at around 1.9 eV. The intensity of the CL emission is very similar for all three different morphologies. The Gaussian deconvolution of the emission bands of necklace-, tower-, and rod-like nanostructures revealed two component bands centered around 1.83 eV (orange band) and 2.23 eV (green band), as shown in Figure 7b–d. No band-edge related emissions were detected for the nanostructures. Although the orange emission is frequently observed in In_2O_3 nanostructures, its origin remains unclear. This emission in In_2O_3 has been associated with interstitial In_i^{3+} sites,[30] and to the defects associated with oxygen vacancies (V_O).[31−33] The green emission has been related to the point defects caused by oxygen excess, such as interstitial oxygen (O_i), indium vacancies (V_{In}), or antisite oxygen (O_{In}) in In_2O_3 lattice.[34] The increase of the relative intensity of orange band (I_o/I_g) with the increase of growth temperature and hence the change of morphology of the In_2O_3 nanostructures (Figure 7b–d) clearly indicate an increase in oxygen vacancy concentration in the nanostructures grown at higher temperatures. As we kept the flow rate of the reaction gas (O_2) during growth of all the samples fixed, a higher evaporation rate of indium precursor at higher growth temperature might have produced In_i^{3+} sites along with oxygen vacancies in higher concentrations.

During deposition, the Au film over the Si substrate breaks down to form Au nanoparticles, which act as preferential nucleation sites in the VLS process. When the rate of saturation of metal droplets and the In_2O_3 deposition (precipitation) are equal, an uniform growth of elongated structures is expected, which usually results in the growth of nanowires, nanobars, nanoribbons, nanorods, etc.[25,35,36] However, when the deposition temperature is not high enough, the rate of incorporation/dissolution of indium oxide in the catalyst droplets and the rate of deposition (precipitation) are different, which leads to the formation of 1D In_2O_3 nanostructures of nonuniform diameters. Such nonuniform growth due to a mismatch of precursor dissolution and compound precipitation has also been observed for SiC,[36] CdO,[37] and CdS,[38] leading to the formation of necklace-like structures in the VLS growth process. The solubility of In_2O_3 in Au catalyst nanodroplets varies with temperature and In_2O_3 concentration in the nanodroplets. Besides, the evaporation rate of metallic indium from the quartz boat and its reaction with O_2 also depend on temperature. Utilizing indium as precursor, Yan et al.[39] obtained tower-like In_2O_3 nanostructures in the VLS growth process, which they associated with the discontinuous (interrupted) supersaturation of catalyst (Au) droplets by the reactant species in the vapor phase. Such a discontinuous supersaturation of the catalyst droplets is also expected in the present case. On reaching the supersaturation limit of the catalyst droplets, unidirectional growth of In_2O_3 starts. As the quantity of the reacting species is limited, the 1D growth process stops until the catalyst droplets attain their supersaturation limit again. During this process, incorporation of vapor species in the lateral surfaces of the nanostructures can also occur via the VS process.

On the basis of the obtained results, and the results reported in the literature, we can conclude that the 1D In_2O_3 nanostructures of the present work grow following the preferential [100] growth direction[17] exposing (111) lateral faces, which are the crystal planes with lower surface energy (γ) (surface energy for indium oxide lower index crystal planes follows the relation $\gamma(111) < \gamma(100) < \gamma(110)$.[40] Because of intermittent saturation of Au catalyst at 825 °C, a reduce growth rate is achieved, and slow formation of stacked octahedra is induced at lateral (111) crystalline planes. For the nanostructures grown at 850 °C, the growth rate is increased, and truncated octahedra are stacked during growth,

DOI: 10.1021/acs.cgd.7b00395
Cryst. Growth Des. 2017, 17, 4596−4602

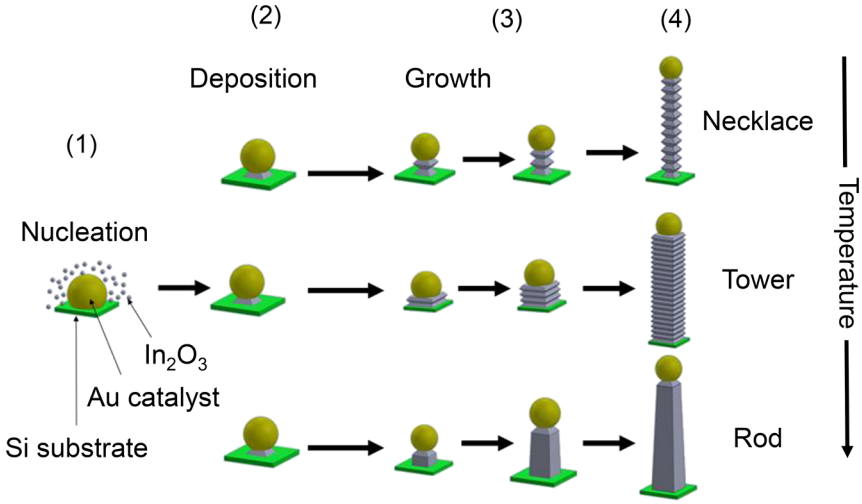

Figure 8. (a) Schematic presentation of the growth steps for 1D nanostructures in the VLS process depending on growth temperature: (1) transport of In_2O_3 to the catalyst, (2) dissolution of precursor at catalyst surface and diffusion inside nanodroplets, (3) precipitation and growth at liquid−solid interface, and (4) final morphology.

producing In_2O_3 nanostructures of stepped surfaces. Finally at 900 °C, the saturation and precipitation rates balance each other, promoting the growth of smooth lateral surfaces, showing a certain ripening or steps in some cases only, as observed in their high-magnification TEM images. Furthermore, a change in growth direction is observed for the nanostructures grown at higher temperatures. Taking into account the highly isotropic cubic structure of indium oxide, the differences in the surface energy of the different crystalline orientations are small,[41] and therefore, alternating growth directions are quite possible. In the present case, the change of growth direction might have been induced at the end of the thermal treatment, when the furnace temperature was cooled down freely, keeping the atmosphere inside saturated in In_2O_3 vapor. The observed tapering of the structures grown at higher temperatures could be due to a simultaneous VS growth of the pregrown nanostructures directly absorbing vapor species at their lateral surfaces or re-evaporation form the convex regions of the pregrown structures. As the convex regions of the nanostructures have higher vapor pressure, at high temperature, the vapor species from these regions diffuse along the lateral surfaces of the nanostructures, filling the concave regions between truncated octahedra, resulting in smooth lateral surfaces, as observed in the rod-like structures. On the other hand, the low saturation rate of the catalyst droplets could cause the surrounding In_2O_3 vapor (in the reaction atmosphere) to be incorporated on the lateral side of the nanostructures through the VS process.[42] The length and width of the nanostructures increase on increasing the growth temperature, as a larger amount of In_2O_3 vapor is available in the reaction atmosphere. The growth processes of the nanostructures with representative morphologies are depicted schematically in Figure 8.

CONCLUSIONS

Well crystalline 1D In_2O_3 nanostructures of necklace-, tower-, and rod-like morphologies could be fabricated in large numbers in a rapid VLS process by controlling the temperature of precursors. The nanostructures grow preferentially along the [100] direction of the body centered cubic lattice. A variation of the growth temperature induces variations in the solubility of a gaseous precursor and the supersaturation limit of metal catalyst droplets, affecting the precipitation/growth process of In_2O_3 nanocrystals. While a lower growth temperature favors the growth of necklace-like structures consisting of well faceted octahedral units due to a slower rate of saturation of catalysts droplets, a higher growth temperature produces continuous rod-like 1D structures with smooth surfaces due to the balance between the rate of dissolution of gaseous precursor, rate of saturation of the catalyst droplet, and the precipitation rate from it. A variation in the rate of dissolution of gaseous precursor or the solubility of catalyst droplet induces interrupted growth of In_2O_3, producing stacked 1D structures. Simultaneous involvement of the VS process not only modifies the final morphology of the VLS grown nanostructures, it also produces In_2O_3 nano- and microstructures of other morphologies, especially at lower growth temperatures.

ASSOCIATED CONTENT

Supporting Information

The Supporting Information is available free of charge on the ACS Publications website at DOI: 10.1021/acs.cgd.7b00395.

SEM images and XRD patterns of the nanostructures (PDF)

AUTHOR INFORMATION

Corresponding Author

*E-mail: upal@ifuap.buap.mx.

ORCID

Umapada Pal: 0000-0002-5665-106X

Notes

The authors declare no competing financial interest.

ACKNOWLEDGMENTS

The work has been financially supported by VIEP-BUAP (Grant No. VIEP/EXC/2017) and DITCo-BUAP (Grant No. DITCo-2016-13), Mexico. J.A.R.R. thanks CONACyT, Mexico, for extending doctoral fellowship (No. 290840).

DOI: 10.1021/acs.cgd.7b00395
Cryst. Growth Des. 2017, 17, 4596−4602

REFERENCES

(1) Wang, J. X.; Xie, S. S.; Gao, Y.; Yan, X. Q.; Liu, D. F.; Yuan, H. J.; Zhou, Z. P.; Song, L.; Liu, L. F.; Zhou, W. Y.; Wang, G. *J. Cryst. Growth* **2004**, *267*, 177.
(2) Kumar, M.; Mehta, B. R.; Singh, V. N.; Chatterjee, R.; Milikisiyants, S.; Lakshmi, K. V.; Singh, J. P. *Appl. Phys. Lett.* **2010**, *96*, 123114.
(3) Seetha, M.; Mangalaraj, D.; Masuda, Y. *Adv. Sci., Eng. Med.* **2011**, *3*, 202.
(4) Liang, C. H.; Meng, G.; Lei, Y.; Phillipp, F.; Zhang, L. *Adv. Mater.* **2001**, *13*, 1330.
(5) Granqvist, C. G. *Appl. Phys. A: Solids Surf.* **1993**, *57*, 19.
(6) Reddy, V. P.; Kumar, A. V.; Swapna, K.; Rao, K. R. *Org. Lett.* **2009**, *11*, 1697.
(7) Wu, C. C.; Wu, C. I.; Sturm, J. C.; Kahn, A. *Appl. Phys. Lett.* **1997**, *70*, 1348.
(8) Zhang, W.; Jie, J.; He, Z.; Tao, S.; Fan, X.; Zhou, Y.; Yuan, G.; Luo, L.; Zhang, W.; Lee, C. S.; Lee, S. T. *Appl. Phys. Lett.* **2008**, *92*, 153312.
(9) Pramod, N. G.; Pandey, S. N.; Sahay, P. P. *J. Therm. Spray Technol.* **2013**, *22*, 1035.
(10) Li, X.; Yao, S.; Liu, J.; Sun, P.; Sun, Y.; Gao, Y.; Lu, G. *Sens. Actuators, B* **2015**, *220*, 68.
(11) Jia, H.; Zhang, Y.; Chen, X.; Shu, J.; Luo, X.; Zhang, Z.; Yu, D. *Appl. Phys. Lett.* **2003**, *82*, 4146.
(12) Wang, B.; Zheng, Z.; Wu, H.; Zhu, L. *Nanoscale Res. Lett.* **2014**, *9*, 111.
(13) Kumar, M.; Singh, V. N.; Mehta, B. R.; Singh, J. P. *J. Phys. Chem. C* **2012**, *116*, 5450.
(14) Hsin, C. L.; He, J. H.; Chen, L. J. *Appl. Phys. Lett.* **2006**, *88*, 063111.
(15) Wu, X.; Wang, Y.; Yang, B. *Appl. Phys. A: Mater. Sci. Process.* **2014**, *117*, 781.
(16) Sabry, R. S.; Agool, I. R.; Mjbel, A. *Optik* **2015**, *126*, 2228.
(17) Li, L.; Chen, S.; Kim, J.; Xu, C.; Zhao, Y.; Ziegler, K. J. *J. Cryst. Growth* **2015**, *413*, 31.
(18) Wang, C. Y.; Dai, Y.; Pezoldt, J.; Lu, B.; Kups, T.; Cimalla, V.; Ambacher, O. *Cryst. Growth Des.* **2008**, *8*, 1257.
(19) Xiangfeng, C.; Caihong, W.; Dongli, J.; Chenmou, Z. *Chem. Phys. Lett.* **2004**, *399*, 461.
(20) Ba, J.; Rohlfing, D. F.; Feldhoff, A.; Brezesinski, T.; Djerdj, I.; Wark, M.; Niederberger, M. *Chem. Mater.* **2006**, *18*, 2848.
(21) Yin, W.; Doty, M.; Ni, C.; Hu, C.; Cao, M.; Wei, B. *Eur. J. Inorg. Chem.* **2011**, *2011*, 1570.
(22) Johnson, M. C.; Aloni, S.; McCready, D. E.; Bourret-Courchesne, E. D. *Cryst. Growth Des.* **2006**, *6*, 1936.
(23) Calestani, D.; Zha, M.; Zappettini, A.; Lazzarini, L.; Zanotti, L. *Chem. Phys. Lett.* **2007**, *445*, 251.
(24) Dai, L.; Chen, X. L.; Jian, J. K.; He, M.; Zhou, T.; Hu, B. Q. *Appl. Phys. A: Mater. Sci. Process.* **2002**, *75*, 687.
(25) Magdas, D. A.; Cremades, A.; Piqueras, J. *Appl. Phys. Lett.* **2006**, *88*, 113107.
(26) Kim, W. J.; Pradhan, D.; Sohn, Y. *J. Mater. Chem. A* **2013**, *1*, 10193.
(27) Bierman, M. J.; Lau, Y. K. A.; Kvit, A. V.; Schmitt, A. L.; Jin, S. *Science (Washington, DC, U. S.)* **2008**, *320*, 1060.
(28) Ramos Ramón, J. A.; León Sánchez, D.; Herrera Zaldívar, M.; Pal, U. *Mater. Sci. Semicond. Process.* **2015**, *40*, 943.
(29) Yin, W.; Su, J.; Cao, M.; Ni, C.; Cloutier, S. G.; Huang, Z.; Ma, X.; Ren, L.; Hu, C.; Wei, B. *J. Phys. Chem. C* **2009**, *113*, 19493.
(30) Kumar, M.; Singh, V. N.; Singh, F.; Lakshmi, K. V.; Mehta, B. R.; Singh, J. P. *Appl. Phys. Lett.* **2008**, *92*, 171907.
(31) Papageorgiou, P.; Zervos, M.; Othonos, A. *Nanoscale Res. Lett.* **2011**, *6*, 311.
(32) Zheng, M. J.; Zhang, L. D.; Li, G. H.; Zhang, X. Y.; Wang, X. F. *Appl. Phys. Lett.* **2001**, *79*, 839.
(33) Yang, H. Y.; Yu, S. F.; Liang, H. K.; Chen, T. P.; Gao, J.; Wu, T. *Opt. Express* **2010**, *18*, 15585.
(34) Mazzera, M.; Zha, M.; Calestani, D.; Zappettini, A.; Lazzarini, L.; Salviati, G.; Zanotti, L. *Nanotechnology* **2007**, *18*, 355707.
(35) Gao, T.; Wang, T. *J. Cryst. Growth* **2006**, *290*, 660.
(36) Hao, Y.-J.; Wagner, J. B.; Su, D. S.; Jin, G.-Q.; Guo, X.-Y. *Nanotechnology* **2006**, *17*, 2870.
(37) Kuo, T. J.; Huang, M. H. *J. Phys. Chem. B* **2006**, *110*, 13717.
(38) Kar, S.; Chaudhuri, S. *J. Phys. Chem. B* **2006**, *110*, 4542.
(39) Yan, Y.-G.; Zhang, Y.; Zeng, H.-B.; Zhang, L.-D. *Cryst. Growth Des.* **2007**, *7*, 940.
(40) Wang, Z. L. *J. Phys. Chem. B* **2000**, *104*, 1153.
(41) Hao, Y.; Meng, G.; Ye, C.; Zhang, L. *Cryst. Growth Des.* **2005**, *5*, 1617.
(42) Yan, Y.; Zhang, Y.; Zeng, H.; Zhang, J.; Cao, X.; Zhang, L. *Nanotechnology* **2007**, *18*, 175601.

DOI: 10.1021/acs.cgd.7b00395
Cryst. Growth Des. 2017, 17, 4596−4602